INTERNATIONAL JOURNAL OF CLIMATOLOGY
Int. J. Climatol. **34**: 964–977 (2014)
Published online 18 June 2013 in Wiley Online Library
(wileyonlinelibrary.com) DOI: 10.1002/joc.3733

RMetS
Royal Meteorological Society

Caribbean low-level jets and accompanying moisture fluxes in a global warming climate projected with CMIP3 multi-model ensemble and fine-mesh atmospheric general circulation models

T. Nakaegawa,[a]* A. Kitoh,[a] Y. Ishizaki,[a†] S. Kusunoki[a] and H. Murakami[a,b]

[a] *Climate Research Department, Meteorological Research Institute, Tsukuba, Japan*
[b] *International Pacific Research Center, University of Hawaii, Honolulu, HI, USA*

ABSTRACT: This study used the third phase of the Coupled Model Intercomparison Project (CMIP3) multi-model ensemble (MME) and atmospheric general circulation models (AGCMs) with three horizontal resolutions, 20, 60, and 180 km, to investigate climate projections of the Caribbean low-level jet (CLLJ) and accompanying moisture fluxes. Future climate simulations were also performed with 60- and 180-km mesh AGCMs forced by four lower boundary conditions both to quantify uncertainty in the CLLJ projections and to determine the physical mechanism of change in the CLLJ. Changes among the CMIP3 MME models in projected CLLJ in the future climate were inconsistent in sign and statistically insignificant, whereas consistently among the models the easterly moisture flux accompanying the CLLJ significantly intensified. The AGCM simulations with three different horizontal resolutions demonstrated that the merits of dynamical downscaling for the CLLJ and moisture flux were limited for climate projections, although the high-horizontal resolution models improved reproducibility of the CLLJ and moisture flux in the present-day climate and can provide spatially detailed projections. Different projected sea surface temperatures (SSTs) as lower boundary conditions of the 60- and 180-km mesh single-AGCM simulations clearly affected changes in the CLLJ. Both the CMIP3 MME analysis and the 60- and 180-km mesh AGCM ensembles showed that large-scale SST patterns between the eastern tropical Pacific and the region from the Caribbean Sea to the western tropical Atlantic influenced changes in the CLLJ in the future climate, as seen in the present-day climate.

KEY WORDS Caribbean low-level jet; global warming; multi-model ensemble; moisture flux; CMIP3; AGCM; high resolution; uncertainty

Received 24 October 2012; Revised 25 March 2013; Accepted 29 April 2013

1. Introduction

Western Hemisphere warm pool (WHWP) with warm waters (>28.5 °C) develops east and west of Central America and Caribbean, and affects the regional climates (Ropelewski and Halpert, 1987; Enfield, 1996). This region is also characterized by the Caribbean low-level jet (CLLJ; e.g. Whyte *et al.*, 2008; Cook and Vizy, 2010). CLLJ has maximum easterly in the lower troposphere around 925 hPa in the Caribbean Sea around 15°N. In the present century, changing climate may noticeably affect the CLLJ (e.g. Taylor *et al.*, 2012) and have larger hydroclimatic consequences; however, because of the region's relatively small landmass area and the difficulty of representing its topography, few attempts have been made to model projections of future climate here.

Located on the southern edge of the North Atlantic Subtropical High (NASH), the CLLJ is influenced by the WHWP; in the present-day Caribbean, the CLLJ influences the interannual variability of wet and dry years (Méndez and Magaña, 2010). The CLLJ has a semi-annual cycle on a seasonal mean timescale: two strong seasons in June–July–August (JJA) and December–January–February (DJF), and two weak seasons in March–April–May (MAM) and in September–October–November (SON). The CLLJ contributes to easterly wave activities (Serra *et al.*, 2010) and affects the vertical wind shear and moisture over the Caribbean (Wang *et al.*, 2008). These local environments control tropical cyclone (TC) formation (e.g. Gray, 1968); therefore, CLLJ is closely linked to TC formation and is a key phenomenon in the Caribbean.

The first climate projection for the Caribbean was made at the end of the 20th century (Singh, 1997); however, according to the Fourth Assessment Report of the Intergovernmental Panel on Climate Change (Christensen *et al.*, 2007), projections for the Caribbean are limited.

* Correspondence to: T. Nakaegawa, Meteorological Research Institute, 1-1 Nagamine, Tsukuba, Ibaraki 305-0052, Japan. E-mail: tnakaega@mri-jma.go.jp

†Current address: National Institute for Environmental Studies, Tsukuba, Japan

The multi-model ensemble (MME) of the third phase of the Coupled Model Intercomparison Project (CMIP3; Meehl *et al.*, 2007) projects a decrease in annual mean precipitation by 9% over most of this region at the end of the 21st century under the Special Report on Emission Scenario (SRES) A1B scenario, accompanied by more frequent dry extremes in all seasons. In all seasons, most models project decreased precipitation in Central America and increased summer precipitation in some parts of northeastern Mexico and over the eastern Pacific (e.g. Angeles *et al.*, 2007). Annual maximum 5-day rainfall and annual maximum number of consecutive dry days were projected to increase in most areas of Central America, Mexico, and the Caribbean with three different horizontal resolution atmospheric global general circulation models (AGCMs) (Nakaegawa et al., 2013a, 2013b).

Karmalkar *et al.* (2011) and Taylor *et al.* (2012) also investigated the CLLJ in the future climate by using a regional climate model (RCM) forced by lower and lateral boundary conditions obtained from one of the CMIP3 models. They found that a strong CLLJ is more likely to persist through November when compared with October in the present-day climate, and will therefore be partly responsible for a decrease in precipitation. Rauscher *et al.* (2008) found in several CMIP3 models of future climate a strong CLLJ that will be responsible in part for intensified mid-summer drought. In addition, Rauscher *et al.* (2011), using an AGCM, examined the influences on a drying Central America of a smaller increase in sea surface temperature (SST) in the tropical North Atlantic compared with the surrounding oceans and show that in the future climate, this regional SST pattern produces a stronger CLLJ.

A projection using a dynamical downscaling approach with a RCM depends on both the lower and the lateral boundary conditions. Moreover, in a RCM it is not possible to alter large-scale features that are determined by the selected CMIP3 model, but the RCM does allow values such as small-scale intensity, location, and distribution to be added. However, the findings presented by Taylor *et al.* (2012) depend solely on the CMIP3 model; when they used the model with dynamical downscaling, an unclear value was added, and the two results were not compared. Rauscher *et al.* (2008, 2011) focused on a drying Central America and did not comprehensively analyse future changes in the CLLJ by using the CMIP3 MME.

In our study, we first projected changes in the CLLJ in future climate by using CMIP3 MME. We assessed the merits of dynamical downscaling for projection of the CLLJ by using high-resolution AGCMs with three horizontal resolutions. With few exceptions (e.g. Giorgi *et al.*, 2009; van der Linden and Mitchell, 2009), projections with dynamical downscaling are usually obtained with an atmosphere–ocean general circulation model (AOGCM). We performed multiple simulations with 60- and 180-km mesh AGCMs forced by four lower boundary conditions to quantify uncertainty in projection of the CLLJ. From these simulations, we investigated a physical mechanism for change in the CLLJ. Although moisture fluxes accompany the CLLJ, they had not yet been projected in future climate, even though moisture fluxes are additional key factors in changes in TC formation and in climate dryness. Here, we projected changes in moisture flux with quantified uncertainty and showed the dependency of the horizontal resolutions on the projections and physical mechanisms between the CLLJ and large-scale SST pattern in the future climate.

2. Model and experimental conditions

2.1. Model

For a global hydrostatic AGCM, we used the Meteorological Research Institute (MRI) AGCM3.1 model, which has been widely used for climate projection studies, for example, for South America (Kitoh *et al.*, 2011; Blázquez and Nuñez, 2013), the East Asia summer monsoon (Kitoh and Kusunoki, 2008), TCs (Murakami *et al.*, 2012), and river discharge (Nakaegawa *et al.*, 2013b).

The AGCM has a triangular truncation at wave number 959 with a linear Gaussian grid in the horizontal, corresponding to a grid spacing of approximately 20 km (T_L959), and 60 layers in the vertical with the model top at 0.1 hPa (MRI-AGCM3.1S). We also used two reduced resolution versions, T_L319 and T_L95, corresponding to grid spacing of 60 km (MRI-AGCM3.1H) and 180 km (MRI-AGCM3.1L), respectively.

The AGCM has many subgrid-scale parameterizations, including the Arakawa–Schubert scheme with a prognostic closure for cumulus parameterization (Randall and Pan, 1993) and the Japan Meteorological Agency's latest simple biosphere model (Sellers *et al.*, 1986; Hirai *et al.*, 2007) for land biosphere–hydrosphere parameterization. Mizuta *et al.* (2006) describes the model in detail.

2.2. Experiments

We performed 25-year simulations for the present-day climate (1979–2003) and the future climate (2075–2099), as listed in Table 1. This type of multiyear climate simulation is called a time-slice experiment (Bengtsson *et al.*, 1996).

We performed present-day climate simulations using three horizontal resolutions, 20, 60, and 180 km. As lower boundary conditions we used the observed monthly SST and sea-ice concentration (HadISST; Rayner *et al.*, 2003). These simulations take a global-scale dynamical downscaling approach and therefore raise no concerns about lateral boundary conditions because of incomplete dynamical and thermal interactions between the outer and the inner domains (e.g. Kanamaru and Kanamitsu, 2007).

We conducted a single 25-year time-slice simulation for 2075–2099 with the 20-km mesh model under the SRES A1B. For the future climate simulation, we used as lower boundary conditions SST data obtained by superposing three components (Mizuta *et al.*, 2008): the

Table 1. Experimental design.

25-Year target period	Grid spacing (km)	Sea surface temperature and sea-ice concentration	Ensemble size
Present day	20	Observation HadISST1	1
1979–2003	60	Observation HadISST1	3
	180	Observation HadISST1	1
Future	20	CMIP3 multi-model ensemble	1
2075–2099	60	CMIP3 multi-model ensemble	3
	60	CSIRO-Mk3.0[a]	3
	60	MIROC3.2 (hi-res)[b]	3
	60	MRI-CGCM2.3.2[c]	3

[a]Commonwealth Scientific and Industrial Research Organisation (CSIRO) Atmospheric Research, Australia. [b]Center for Climate System Research (University of Tokyo), National Institute for Environmental Studies, and Frontier Research Center for Global Change (FRCGC) of Japan Agency for Marine-Earth Science and Technology (JAMSTEC), Japan. [c]Meteorological Research Institute, Japan.

future change in the MME of SST projected from a multi-model data set, the trend in the MME of SST, and the detrended observed SST anomalies for the period 1979–2003. The MME consisted of 18 CMIP3 GCMs as listed in Table 1 of Mizuta *et al.* (2008). The future change in the MME of SST was determined as the difference between the present-day and the future climate simulations under SRES A1B; it shows an El Niño-like pattern in the tropical Pacific (IPCC, 2007) and small increases in the southern WHWP compared with the surrounding oceans. The resulting SST data for the future climate simulation have a higher mean and a clear increasing trend, but also include a time series of observed variabilities including El Niño–Southern Oscillation (ENSO) events. Because ENSO projections are not in agreement among the CMIP3 models in the Fourth Assessment Report (IPCC, 2007), the use of observed variabilities may be one of the best possible choices. Future sea-ice concentration was obtained in a similar fashion. The prescribed change in global annual mean 25-year averaged SST was 2.16 °C. Schematics of the process by which we developed these lower boundary conditions are given by Mizuta *et al.* (2008) and Kitoh *et al.* (2009, 2011). We used initial conditions obtained from previous 20-km mesh simulations (Mizuta *et al.*, 2006) for both the present-day and the future climate simulations. Spin-up time was 14 months for each simulation.

Dynamical downscaling is a strong tool for obtaining small-scale climatic and atmospheric phenomena, but the approach does not necessarily provide better or additional information about the CLLJ. Moreover, uncertainty is inherent in current climate change projections. The pattern of SST increase in the tropics and subtropics affects regional response in the future climate (Clement *et al.*, 2010; Xie *et al.*, 2010), and the local spatial pattern of changes in SST influences precipitation decrease in Central America and the Caribbean (Rauscher *et al.*, 2011). To quantify both of these uncertainties in climate change projections, we performed ensemble simulations with the 60-km mesh model. The ensemble was composed of simulations with three different data sets in addition to the MME SST and sea-ice concentrations used in the 20-km mesh model simulation: SSTs and sea-ice concentrations of the CSIRO-Mk3.0 (CSIRO), MIROC3.2(hires) (MIROC), and MRI-CGCM2.3.2 (MRI) models. These models prescribed changes in global annual mean 25-year averaged SST of 1.43, 1.73, and 3.49 °C, respectively. For climatological annual mean changes, CSIRO-Mk3.0 and MRI-CGCM2.3.2 SSTs show an El Niño-like pattern, with the eastern equatorial SST rising more than the western equatorial SST as in the MME of SST, whereas the MIROC3.2 (hi-res) SSTs show a La Niña-like pattern. Although these patterns resemble those of El Niño and La Niña events, the physical mechanisms differ (Collins *et al.*, 2010). In addition, MIROC3.2(hires) and MRI-CGCM2.3.2 show a larger SST increase in the tropical eastern North Atlantic than in the Caribbean Sea and tropical western North Atlantic; this is seen in the CMIP3 MME SST data set used in this study and can be seen in those of most CMIP3 models (see Figure 16 in Murakami and Wang, 2010). For each of these four SSTs, we performed three-member simulations, thus making up a 12-member (4×3) ensemble, with differing initial conditions to assess the influence of natural variability.

2.3. CMIP3 MME

We used 17 climate models from the CMIP3 MME for projections of the CLLJ in future climates because of the 18 CMIP model outputs used for the lower boundary conditions, 1 was not available. The present-day climatologies for 1979–1999 were obtained from the 20th-Century Climate in Coupled Models experiment (20C3M) as part of CMIP3. Historical observations of greenhouse gases, sulphate aerosols, and solar and volcanic forcings were used for the present-day climate simulations. The future climatologies for 2075–2099 were obtained from the CMIP3 experiment under the SRES A1B scenario (IPCC, 2000). This scenario is characterized by medium–high carbon emissions and carbon dioxide concentrations of 700 ppm by the end of the 21st century. We used a single member of each model or the first member in this analysis even when multiple members were available for a CMIP3 model.

2.4. Observational data

We compared winds and moisture fluxes between the 25-year Japanese Reanalysis (JRA25; Onogi *et al.*, 2007) and the model simulations. The horizontal resolution of the JRA25 data set is a triangular truncation at wave number T109 with a Gaussian grid in the horizontal, corresponding to a grid spacing of approximately 120 km (T106), and the temporal resolution is 6 h. As an index of the CLLJ, we used anomalous westerly (zonal wind at 925 hPa averaged over 70°W–80°W, 12.5°N–17.5°N, referred to as the CLLJ index area; Taylor *et al.*, 2012). For the same purpose, we also used data from the European Centre for Medium-Range Weather Forecasts Reanalysis–Interim (ERA–Interim; Dee *et al.*, 2011). In Section 4, we discuss future changes on a 3-month mean timescale.

2.5. Statistical methods

We applied a Bayesian model averaging to determine model weightings (Tebaldi *et al.*, 2005), in addition to a simple averaging, called arithmetic ensemble mean (AEM).

In this method, MME means $\tilde{y}$ were determined as

$$\tilde{y} = \sum_{i=1}^{17} w_i y_i \tag{1}$$

where w_i is the weight for each model and y_i is the simulated value by model i. Because Bayes factors can be interpreted as model weights, as suggested by Kass and Raftery (1995), previous research (Min and Hense, 2006; Ishizaki *et al.*, 2010, 2012) used Bayes factors to produce weighted MMEs of climate models. The metrics we used to evaluate model skills and to produce model weights as Bayes factors were climatological seasonal means (DJF and JJA) and the standard deviations of climatological interannual variations of 925-hPa zonal wind averaged over the CLLJ index area during 1979–2003.

A brief explanation of Bayes factors is first required. The Bayes factors B_{jr} of model m_j with respect to reference model m_r are expressed as

$$B_{jr} = \frac{P\left(m_j|d\right)/P\left(m_r|d\right)}{P\left(m_j\right)/P\left(m_r\right)} \tag{2}$$

where d is observational data, $P(m_j)$ and $P(m_r)$ are prior distributions of model m_j and the reference model m_r, respectively, and $P(m_j|d)$ and $P(m_r|d)$ are posterior distributions of model m_j and the reference model m_r, respectively. We assumed that the prior distributions of model m_j were identical to the prior distribution of the reference model m_r. Therefore, we estimated the Bayes factors as the likelihood ratio, expressed as

$$B_{jr} = \frac{l\left(d|m_j\right)}{1\left(d|m_r\right)} \tag{3}$$

where the likelihood in model m_j was assumed to be normally distributed and is expressed as

$$1\left(d|m_j\right) = \frac{1}{\sqrt{2\pi\left(\sigma_o + \sigma_{mj}\right)}} \exp\left(-\frac{\alpha_j}{2}\right) \tag{4}$$

where σ_o and σ_{mj} are the variances of the observations and model j, respectively, and α_j is the generalized Mahalanobis distance between the observation and model simulation, expressed as

$$\alpha_j = \frac{\left(d - m_j\right)^2}{\sigma_o + \sigma_{mj}} \tag{5}$$

The observational variance σ_o was assumed to be identical to the model variance σ_{mj}, and α_j was assumed to be zero for the reference model m_r, as in Min and Hense (2006). Because the prior distributions were assumed to be identical for all models, the weighting factor of each model w_j could be calculated as the ratio of likelihood for model m_j to the summation of likelihoods for all models. Thus, it can be expressed as

$$w_j = 1\left(d|m_j\right) / \sum_{i=1}^{17} 1\left(d|m_i\right) \tag{6}$$

To produce the model weights from the correlation coefficients of interannual variations, we calculated the weight w_j of each model by

$$w_j = \mathrm{Cor}_j / \sum_{i=1}^{17} \mathrm{Cor}_i \tag{7}$$

where Cor_j is the interannual correlation coefficient of 925-hPa zonal wind averaged over the CLLJ index area for each season between each model and observation during 1979–2003.

3. Reproducibility

We compared the variation of the 3-month mean 925-hPa zonal wind averaged over the CLLJ index area (Figure 1). Both JRA25 and ERA–Interim strongly resembled this variation in phase and magnitude. The 20-km mesh model captured the seasonal variations of the CLLJ, such as DJF and JJA maximums, but did so 1 month earlier than the JRA25 and ERA–Interim. The 20-km mesh model, however, failed to capture the second minimum in MAM and produced a larger amplitude for the 3-month mean 925-hPa zonal wind. The 60- and 180-km mesh models produced very similar seasonal variations, and both failed to capture the maximum in JJA. Different CMIP3 models show very different seasonal variations; however, the CMIP3 MME mean exhibited seasonal variations similar to those of the MRI-AGCMs with a smaller amplitude than that of the JRA25 and ERA–Interim. The seasonal variations of zonal moisture flux resembled

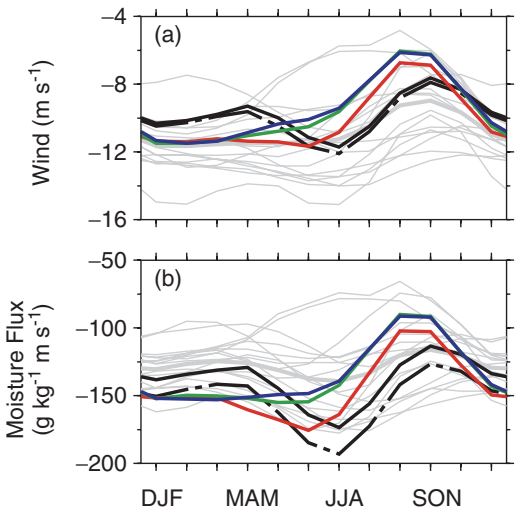

Figure 1. Seasonal variation of climatological seasonal mean 925-hPa zonal wind (a) and moisture fluxes (b) averaged over the CLLJ index area. Black solid and chain, thin grey, and thick grey lines represent JRA25, ERA, each of the CMIP3 models, and CMIP3 MME mean, respectively, while red, green, and blue lines represent the 20-, 60-, and 180-km mesh models, respectively.

those of the zonal wind (Figure 1). The phases of both JRA25 and ERA–Interim coincided, but the easterly zonal moisture flux of JRA25 was weaker compared with that of ERA–Interim because of a slightly weaker CLLJ and less atmospheric moisture. The 20-km mesh model captured well the seasonal variations and the maximum in JJA, but it produced a larger easterly zonal moisture flux from December to June compared with JRA25 and ERA–Interim. The CMIP3 MME mean showed small biases in August–September–October (ASO) to MAM, but it failed to capture the amplitude of the seasonal variation and the maximum in JJA in magnitude. The intensities of zonal moisture flux in all of these models more closely resemble those of JRA25 than those of ERA–Interim.

The maximum easterly zonal wind of the CLLJ has exceeded $13\,\mathrm{m\,s^{-1}}$ during summer (JJA) in the lower troposphere around 925 hPa (e.g. Mo and Higgins, 1996); in the JRA25 data set this maximum was $12\,\mathrm{m\,s^{-1}}$ near 15°N (Figure 2(a)). The CLLJ had a vertically standing structure from the surface to 600 hPa. A westerly zonal wind prevailed north of 30°N. A strong easterly zonal moisture flux accompanied the CLLJ and extended north of the Greater Antilles or Jamaica and eastern Cuba, which appear as two peaks in the lower troposphere in high-resolution regional analyses (Cook and Vizy, 2010); the 20-km mesh model captured these features fairly well, but compared with JRA25, the maximum zonal wind for the CLLJ was weaker (Figure 2(d)). The 60-km mesh model captured the maximum zonal wind, but compared with that in the 20-km mesh model it was even weaker (Figure 2(c)). The 180-km mesh model yielded the weakest maximum zonal wind of the three models and showed the zonal moisture flux smoothly extending to the north without the two peaks described above (Figure 2(b)). These results show that, compared with lower resolution models, the higher resolution model better captured the CLLJ and accompanying moisture fluxes in terms of quantity.

Some of the CMIP3 models also reproduced features of the CLLJ fairly well. CSIRO captured the intensity and the vertical position of the maximum zonal wind of the CLLJ (Figure 2(e)); however, the CLLJ was confined below 800 hPa in the lower troposphere. MIROC, with the highest horizontal resolution among the CMIP3 models, approximately 125 km, captured the two peaks with slight overestimation and also captured the vertical position (Figure 2(f)). MRI captured the CLLJ well except for the vertical level (Figure 2(g)). Among the CMIP3 models, CCSM3.0 developed by National Center for Atmospheric Research showed the best reproducibility for annual mean intensity and seasonal variation of the anomalous westerly (Figure 2(h)), when we used the CLLJ index as the metric. However, the CLLJ was confined below 700 hPa, and its structure was inclined below 850 hPa. Therefore, given all of the above, the CMIP3 models captured the basic features of the CLLJ, which thus allowed us to project changes in the CLLJ in the future climate.

4. Projections

4.1. CMIP3 MME

The 3-month mean 925-hPa zonal wind was projected to change little for all seasons (Figure 3(a)). In contrast, except for July–August–September (JAS) and November–December–January (NDJ) the accompanying 3-month mean easterly moisture flux was projected to increase significantly owing to an increase in saturated specific humidity in a warm climate (Figure 3(b)). Insignificant changes were primarily owing to a weakened CLLJ for JAS (Figure 3(a)) and large uncertainty for NDJ (Figure 3(b)). Although the CLLJ is central to uncertainties in projections of future climate, the easterly moisture flux accompanying the CLLJ will be significantly intensified in a future climate because the increase in the atmospheric water vapour holding capacity is associated with a robust increase in atmospheric temperature.

Future changes in the seasonal mean 925-hPa zonal wind were plotted as a function of annual mean biases and temporal correlation of the seasonal variations of the wind for the CMIP3 models in Figure 4. This figure shows the relationship between the changes in the future climate and the reproducibilities in the present-day climate. The three CMIP3 models with temporal correlation values greater than 0.9 projected a weakened CLLJ for DJF in the future climate, whereas the five CMIP3 models with biases less than $1\,\mathrm{m\,s^{-1}}$ projected consistent but insignificant intensified CLLJ except for one model with weakened CLLJ (Figure 4(a)). For JJA, the five CMIP3 models projected consistent intensified CLLJ, whereas the three CMIP3 models projected inconsistent CLLJ changes:

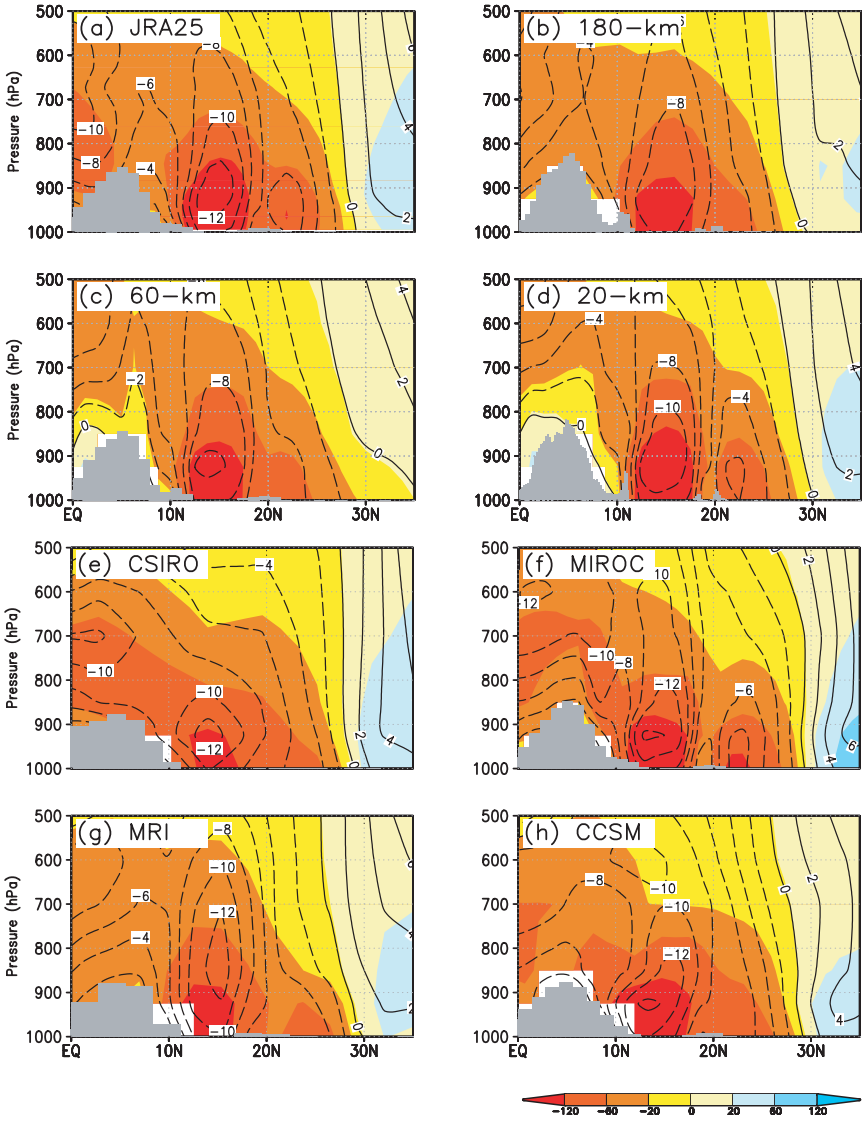

Figure 2. Vertical cross sections showing climatological seasonal mean of zonal moisture flux ($g\,kg^{-1}\,m\,s^{-1}$; colours) and zonal wind (contours in $2\,m\,s^{-1}$ intervals) averaged for 73°W–77°W for JJA. (a) Observations from JRA25; models with (b) 180-, (c) 60-, and (d) 20-km mesh; (e) CSIRO; (f) MRIOC; (g) MRI; and (h) CCSM. Contour. Solid and dashed lines represent positive (westerly) and negative (easterly), respectively. Topographic highs (grey) are South America near the equator and the Greater Antilles near 20°N.

one model with intensified CLLJ and two models with weakened CLLJ (Figure 4(b)). The numbers of intensified CLLJ for DJF and JJA among the CMIP3 models were 8 and 7, respectively, out of the total of 17. The 20-km mesh model and CMIP3 AEM consistently projected intensified CLLJ for DJF but not for JJA, although the two show good reproducibilities in bias and temporal correlation.

The seasonal mean 925-hPa zonal easterly moisture flux consistently increased in the future climate for both DJF and JJA (Figure 5). Although changes in the CLLJ itself were inconsistent, the consistent increase in the seasonal mean 925-hPa zonal easterly moisture flux was caused by a distinct increase in specific humidity because of air temperature rise, as described by the Clausius–Clapeyron relation. The larger increase in the flux for JJA compared with DJF was owing to a stronger CLLJ and more humid atmosphere during the former period. For the annual mean biases and temporal correlation of the seasonal mean 950-hPa moisture flux, no systematic increases in magnitude were projected. The 20-km mesh model has a smaller bias than the CMIP3 AEM, whereas the CMIP3 AEM has better temporal correlation than the 20-km mesh model. The moisture flux in the 20-km mesh model increased more for both the seasons than in the CMIP3 AEM because of larger changes in CLLJ in the 20-km mesh model than in the CMIP3 AEM as seen in Figure 4.

We estimated a MME mean change weighted by the two approaches described in Section 2.5.: a normalized Bayes factor (Min and Hense, 2006) and a normalized temporal correlation (Ishizaki *et al.*, 2012). The MME means of seasonal mean 925-hPa zonal wind with the Bayes factor approach are almost zero for both DJF

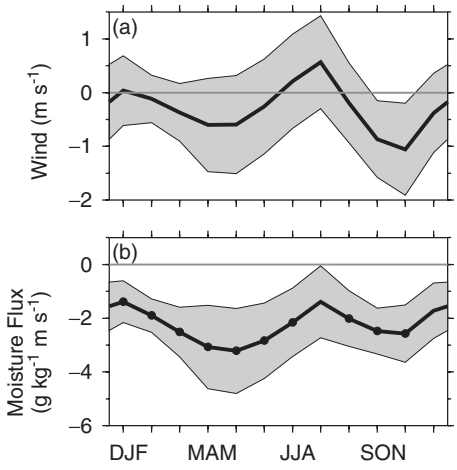

Figure 3. CMIP3 MME mean changes in 3-month mean 925-hPa zonal wind (a) and moisture fluxes (b) averaged over the CLLJ index area. Grey shaded areas represent the confidence interval of the standard deviation, while black circles represent statistically significant changes at 95% confidence level.

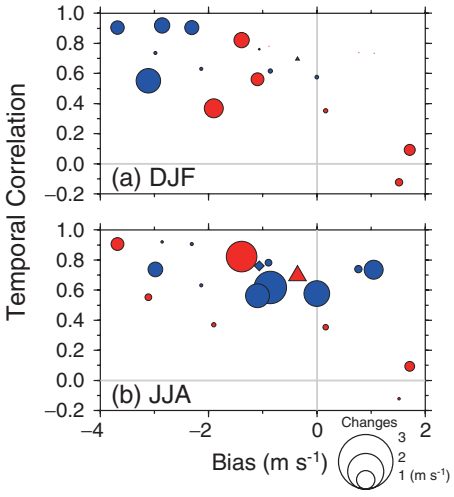

Figure 4. Future changes in seasonal mean 925-hPa zonal wind averaged over the CLLJ index area as a function of its annual mean biases and temporal correlation of the seasonal variation. (a) DJF and (b) JJA. Circles, diamonds, and triangles represent CMIP3 models, CMIP3 AEM, and 20-km mesh MRI-AGCM, respectively, while blue and red represent positive and negative changes, respectively. Symbol size represents magnitude of changes.

and JJA (Table 2). For DJF the MME mean with the normalized temporal correlation approach is nearly the same as AEM, but for JJA the AEM is distinctly larger in magnitude than the means obtained by the AEM and Bayes factor approaches. The means of seasonal mean 925-hPa moisture flux with the temporal correlation approach are similar to those of AEM, whereas those of the Bayes factor approach are approximately half the value of those of the other two approaches. Therefore, we were unable to obtain robust results for the changes in the CLLJ from CMIP3 MME; however, we did observe a significant increase in moisture flux accompanying the CLLJ.

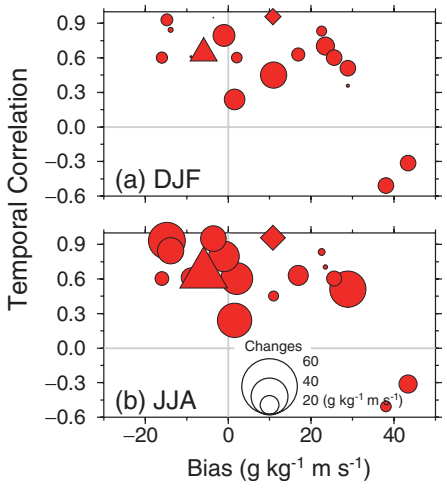

Figure 5. Future changes in seasonal mean 925-hPa zonal moisture flux averaged over the CLLJ index area as a function of its annual mean biases and temporal correlation of the seasonal variation. (a) DJF and (b) JJA. Circles, diamonds, and triangles represent CMIP3 models, CMIP3 AEM, and 20-km mesh MRI-AGCM, respectively. Symbol size represents magnitude of changes.

Table 2. MME mean changes weighted by the two approaches—Bayes factor and normalized temporal correlation—in addition to arithmetic ensemble mean (AEM). Here, * and ** represent a significant changes at 90% and 95% confidence levels, respectively, for AEM.

925-hPa zonal		AEM	Bayes factor	Correlation
Wind ($m\,s^{-1}$)	DJF	0.04	0.00	0.18
	JJA	0.21	0.08	0.25
Moisture flux ($g\,kg^{-1}\,m\,s^{-1}$)	DJF	-13.8^{*}	−6.3	−12.2
	JJA	-21.5^{**}	−10.3	−23.8

4.2. Dependency of the horizontal resolutions

Dynamical downscaling is a strong methodology for obtaining spatially high-horizontal-resolution information about climate projections because it enables more detailed representation of land–sea contrasts, vegetation cover, and topography, and it offers better representation of synoptic and mesoscale atmospheric processes (Kjellstorm and Giorgi, 2010); however, improvements depend greatly on the type of application and the model variables being analysed.

We examined climatological seasonal mean changes in zonal wind and moisture flux between present-day and future climates at the three horizontal resolutions of MRI-AGCM3.1 forced by the CMIP3 MME mean SST (Figure 6). The vertical cross sections clearly depict a change in the CLLJ near 15°N. For DJF, the low-level easterly moisture flux in the CLLJ region was projected to be significantly enhanced by approximately $20\,g\,kg^{-1}\,m\,s^{-1}$ in the 20-km mesh model, although the CLLJ itself was not enhanced (Figure 6(c)). While the 60-km mesh model projected the same general features (Figure 6(b)), it did

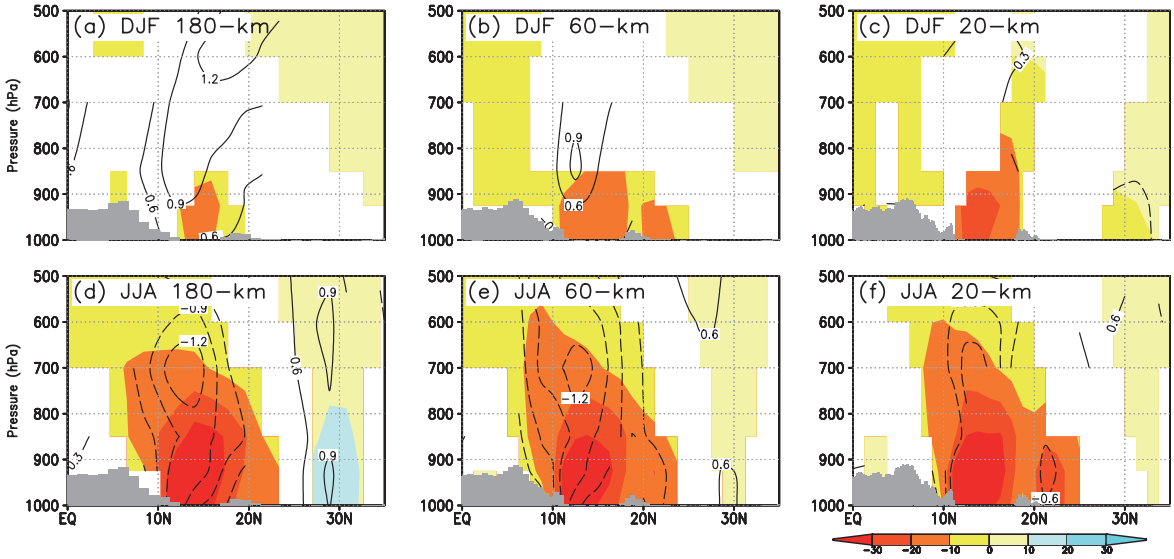

Figure 6. Vertical cross sections showing climatological seasonal mean change of zonal moisture flux ($g\,kg^{-1}\,m\,s^{-1}$; colours) and zonal wind (contours in $0.3\,m\,s^{-1}$ intervals) averaged for 75°W–77°W for DJF in the (a) 180-, (b) 60-, and (c) 20-km mesh models, and for JJA in the (d) 180-, (e) 60-, and (f) 20-km models, where CMIP3 MME mean SST is used as a lower boundary condition. Solid and dashed lines represent positive (westerly) and negative (easterly) anomalies, respectively. Only areas of change that are statistically significant at the 95% level are shown.

not show the same magnitude of moisture flux enhancement as in the 20-km mesh model. The 180-km mesh model projected enhanced easterly moisture flux in the lower atmosphere of the CLLJ region and significantly weaker zonal easterly wind extending from the CLLJ region to the mid troposphere around 25°N (Figure 6(a)).

For JJA, the 20-km mesh model projected a zonal easterly moisture flux that was significantly enhanced in two peaks in the lower troposphere (Figure 6(f)). The CLLJ was projected to be intensified insignificantly in the future climate compared to the present-day climate, and the zonal easterly wind above 800 hPa was projected to be intensified significantly. Projections of the CLLJ in the 60- and 180-km mesh models were similar to those of the 20-km mesh model, but with statistical significance. Change was observed in the seasonal mean zonal wind at 925 hPa as the CLLJ index in the 60- and 180-km mesh models; this change was statistically significant because of the three-member ensemble for each projected SST simulations. Changes in easterly moisture flux greater than $10\,g\,kg^{-1}\,m\,s^{-1}$ extended to 600 hPa near 10°N in the 20- and 60-km mesh models, but in the 180-km mesh model these were confined to below 650 hPa. The different horizontal resolution models show different projections of both the CLLJ and accompanying moisture fluxes in the future climate quantitatively but similar projections qualitatively. From these results, dynamical downscaling may add restricted values for the CLLJ and the moisture flux when the index and the vertical cross section are used for projections. Dynamically downscaled features of the CLLJ in Taylor *et al.* (2012) are very similar to those of one of the CMIP3 models, the HadAM3P developed by Hadley Center, U.K. Met Office, which provides the boundary conditions for the RCM they used.

4.3. Dependency of projected SSTs

Using the four-SST-ensemble results with both the 60- and 180-km mesh models, we investigated the dependency on the projected SSTs. Vertical cross sections were obtained for the four-SST-ensemble means of zonal wind and moisture flux and for consistency of changes in sign (Figure 7). Consistency was defined as consistent agreement between the four-SST-ensemble results and the changes in sign. In DJF, the CLLJ and the easterly moisture flux in the future climate would be weakened consistently among both the 180- and 60-km mesh model ensembles (Figure 7(a) and (c)), although the consistent changes in the easterly moisture flux were confined to below 950 hPa in the 180-km and 850 hPa in the 60-km mesh models (Figure 7(b) and (d)). In JJA, the CLLJ showed no consistent intensification in the 180- and 60-km mesh model ensembles (Figure 7(f) and (h)). Among the four SST ensembles, CLLJ simulated with only the MRI SST was weaker in the future climate compared with the present-day climate, but this difference was not statistically significant, whereas the three others were significantly stronger in the future climate than in the present-day climate. The choice of AOGCM for obtaining the lower boundary conditions determined the result of outputs from the AGCM, and probably from the RCMs, because simulations with the RCMs were constrained by the lateral boundary as well as the lower boundary conditions. The accompanying easterly moisture flux was consistently intensified in the 180-km mesh model simulations, but was not consistently intensified in the 60-km mesh model simulations. This result again indicates the

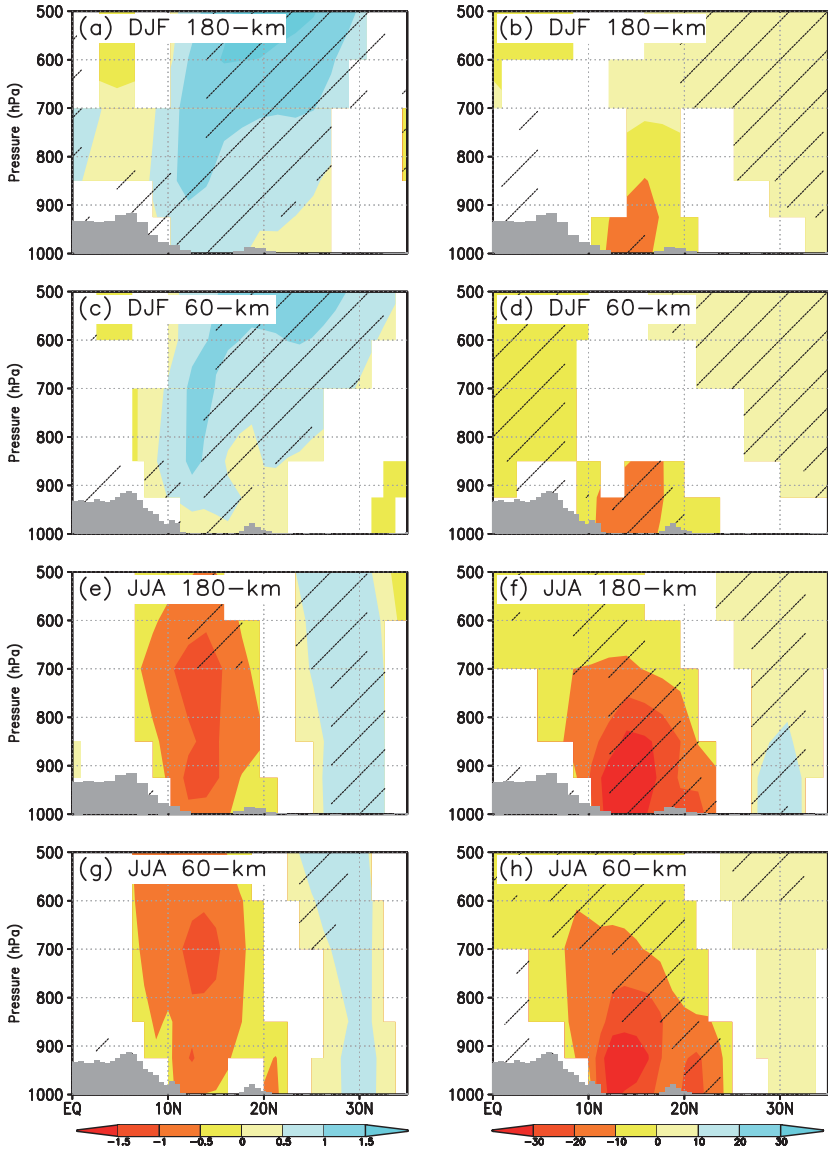

Figure 7. Vertical cross sections showing the four-SST-ensemble means of climatological seasonal mean change of zonal wind ($m\,s^{-1}$) (left) and moisture flux ($g\,kg^{-1}\,m\,s^{-1}$) (right) averaged for 75°W–77°W for DJF in the 180- (a and b) and 60-km (c and d) mesh models, and for JJA in the 180- (e and f) and 60-km (g and h) mesh models. Coloured areas have statistically significant changes at the 95% level. Hatched areas are where all four of the SST ensemble of the 60-km mesh AGCM yielded consistent changes in sign.

importance of the horizontal resolution for the projections at which the target phenomena can be reasonably simulated.

We observed the climatological mean changes in SST and in the 925-hPa geopotential height for JJA in the future climate (Figure 8). For all SST ensemble simulations except MRI, the changes in SST were higher in the eastern tropical Pacific than in the WHWP. The changes projected in the 925-hPa geopotential height by MRI were the smallest among the four models. In the present-day climate, the CLLJ is intensified through the relationship between the meridional geopotential height gradient and jet, corresponding to the westward extension of the NASH (Whyte *et al.*, 2008), when SST anomalies form a warm-Pacific–cool-Atlantic pattern (Wang *et al.*, 2007; Munoz *et al.*, 2008). These observations explain why our simulations with MRI lower boundary condition showed inconsistent change in sign.

4.4. Relationship between the CLLJ and large-scale SST pattern

We further investigated the relationship in changes between the CLLJ and a large-scale SST pattern by using 17 CMIP3 MME projections. As an index of the large-scale SST pattern, we used the SST difference between the eastern tropical Pacific Nino3 region (90°W–150°W, 5°S–5°N) and the region from the Caribbean Sea to the western tropical Atlantic (40°W–80°W, 10°N–20°N) corresponding to the southern WHWP. The climatological seasonal march of the SST difference shows the maximum with positive value in February–March–April and the minimum with

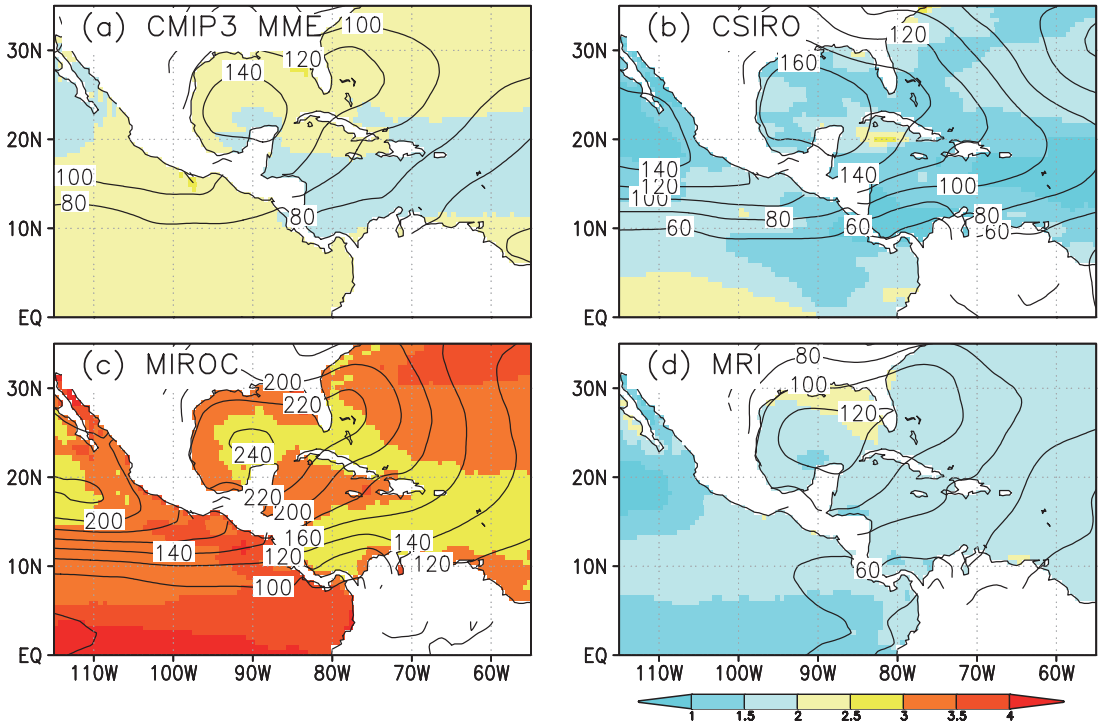

Figure 8. Seasonal mean 925-hPa geopotential height changes (contours in 20-m intervals) and SST changes (K; colours) for JJA in the future climate from the present-day climate. (a) CMIP3 MME, (b) CSIRO, (c) MIROC, and (d) MRI.

negative value in August–September–October. As the SST difference increased, anomalous 3-month mean 925-hPa zonal wind strengthened during DJF, with a significant correlation with SST (coefficient of 0.47; Figure 9(a)). Weakened and poleward-expanded Hadley circulation in the future climate (Lu *et al.*, 2007) produced positive zonal wind changes owing to Matsuno–Gill-type response (Matsuno, 1966; Gill, 1980) seen in Figure 6(a)–(c), and especially Figure 7(a) and (c) where larger positive changes are seen in lower pressure levels. The change in the SST differences modulates the local Hadley circulation and therefore shows positive correlation to the change in CLLJ in DJF. During JJA, anomalous easterlies or CLLJ showed a significant negative correlation with SST (coefficient of −0.58; Figure 9(b)). For both these seasons, the correlations between the 925-hPa zonal wind and the SST difference for both the 60- and 180-km mesh AGCM ensembles were significant. Wang *et al.* (2007) performed an AGCM experiment forced with prescribe observed SST without WHWP and demonstrated that NASH is intensified in JJA. The positive change in the SST difference in the future climate reduces the absolute value of SST differences, weakening the effect of WHWP on NASH. Therefore, CLLJ is intensified and the negative correlation in JJA is obtained.

The relationships between the projections of the two models differing in horizontal resolution closely resembled each other. The results from the CMIP3 MME demonstrate a robust relationship among the differing structures of the models, and the results from the AGCM ensembles also clearly demonstrate the

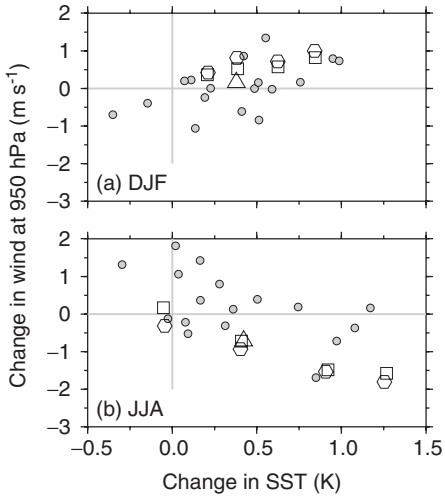

Figure 9. Changes in 925-hPa zonal wind in the future climate against changes in the SST difference (ΔSST) between the eastern tropical Pacific Nino3 region and the region from the Caribbean Sea to the western tropical Atlantic. Grey circles represent CMIP3 models, while triangles, squares, and hexagons represent the 20-, 60-, and 180-km mesh models, respectively.

relationship. Therefore, the relationship was shown to exist in the CMIP3 MME and in a single-AGCM ensemble, suggesting an underlying physical mechanism for the relationship.

Changes in SST in the future climate were smaller in the western tropical Atlantic than in the surrounding latitudes, which increased the zonal gradient of SST and affected the CLLJ. This strengthening of the

CLLJ is seen over the Central American isthmus and the Caribbean Sea in high-resolution models of CMIP3 such as MIROC. The slight SST warming in the tropical North Atlantic relative to the surrounding tropical waters reduces negative diabatic heating in the upper troposphere and excites a Matsuno–Gill-type response (Matsuno, 1966; Gill, 1980), enhancing the NASH as well as its westward extension (Wang *et al.*, 2007). This enhancement strengthens the CLLJ and suggests that the relationship holds under different global mean surface air temperature rises, which is known in the present-day climate as the interannual relationship between the intensity of the CLLJ and a warm-Pacific–cool-Atlantic SST pattern (Wang *et al.*, 2007). The SST differences were projected to increase for both DJF and JJA seasons with high consistency among the CMIP3 MME: 15 of 17 for both the seasons (Figure 9). Therefore, the CLLJ in the future climate would be intensified in JJA and weakened in DJF as long as the CMIP3 MME correctly projected the sign of the change in the SST difference.

5. Discussion

The 20- and 60-km mesh MRI-AGCMs and CMIP3 MME mean fail to capture second minima in MAM. In observation, meridional SST gradients are closely related to CLLJ through meridional sea surface pressure gradients, and positive ocean–atmosphere feedback maintains the CLLJ (Wang 2007). A primary possible common reason for this failure in the both is weak minima. In the MRI-AGCM present-day climate experiments, meridional SST gradients are prescribed; therefore, the feedback lacking in the experiment may contribute to this failure. In contrast, CMIP3 models can treat the feedback. However, coarse horizontal resolutions of CMIP3 models hinder sharp meridional SST gradients and therefore may contribute to this failure. In addition, about one-third CMIP3 models captured the second minima, but did not always show good reproducibilities in bias and temporal correlation.

In extreme dry years in the present-day climate, the NASH expands equatorward and westward, the CLLJ strengthens, and the Intertropical Convergence Zone over the eastern Pacific does not migrate north (e.g. Hastenrath, 1978); these patterns resemble those of the projected future climate. More moisture was projected to be transported in the CLLJ region (Figure 10), but vertically integrated moisture flux convergence was projected to decrease (Figure 10(b) and (d)). Easterly moisture flux travels through this domain to the Pacific without convergence. Therefore, CMIP3 MME analysis (Neelin *et al.*, 2006) and RCM analysis (Campbell *et al.*, 2011; Taylor *et al.*, 2012) consistently show a drying trend. The difference in change in convergence between JJA and DJF is owing to weakening but poleward expansion of the Hadley circulation (Lu *et al.*, 2009). These changes bring dryer future climate in Central America and the Caribbean. Weak divergences in JJA (Figure 10(c)) in the CLLJ region in the present-day climate can be intensified (Figure 10(d)) in the dryer climate, whereas strong divergence in DJF (Figure 10(a)) in the present-day climate cannot be intensified in the future climate. Strong divergences are seen in DJF in Figure 10(a). In addition to the uncertainty in the CMIP3 MME stemming from model structures, our study considered the uncertainties in future climate projections stemming from horizontal resolution, different projected SSTs and sea-ice concentrations, and natural variability in a single AGCM. Although the 20-km mesh model is a powerful tool for global climate change studies, its computational demands rule out its use in ensemble experiments. Therefore, we performed ensemble experiments with the 60- and 180-km mesh models using four different SSTs and sea-ice concentrations and three different initial conditions. The total of 12 ensemble simulations in the future climate for each model enabled us to quantify the uncertainties in future climate projections.

High-resolution AGCM downscaling allows us to explore influences of remote forcings outside a target region through teleconnections on phenomena there. The relationship between the CLLJ and large-scale SST pattern may be a typical case. The same but for RCM restricts our exploration to relationships in the target region because the size of the target region is limited because of computer resources and the remote forcings are implicitly embedded in the lateral boundary conditions. Although it requires huge computer resources, the high-resolution AGCM downscaling is the best approach to exploring the remote forcings such as the relationship between the CLLJ and large-scale SST pattern.

Owing to limited computer resources, dynamical downscaling for a specific region is performed with an RCM forced by the boundary conditions of a CMIP3 (e.g. Taylor *et al.*, 2012) or with multi-RCMs (e.g. Ishizaki *et al.*, 2012). Results from a CMIP3 MME model are not reliable (Figures 1(a), 4, and 9 and Table 2). Our results (Figure 7(f) and (h)) suggest that a multi-GCM and multi-resolution (probably multi-RCM) approach is essential for quantifying the uncertainty even under an emission scenario. Such awareness has led to multi-GCM and multi-RCM simulations for Europe in the ENSEMBLES project (van der Linden and Mitchell, 2009) and to the Coordinated Regional Downscaling Experiment (CORDEX) for the globe (Giorgi *et al.*, 2009). The dynamically downscaled outputs from these projects will allow us to quantify the uncertainty and to raise the reliability of future climate projections.

In designing this high-resolution AGCM downscaling experiment, we assumed that land cover and oceanic phenomena such as ENSO do not change in the future climate. However, changes in cropping and cultivation areas and changes in carbon fertilization effects alter the land cover qualitatively and quantitatively, which influences climate projections (e.g. Salazar *et al.*, 2007). ENSO influences climate variability in this region in the present-day climate (e.g. Giannini *et al.*, 2000). The projected change in ENSO is highly variable among the

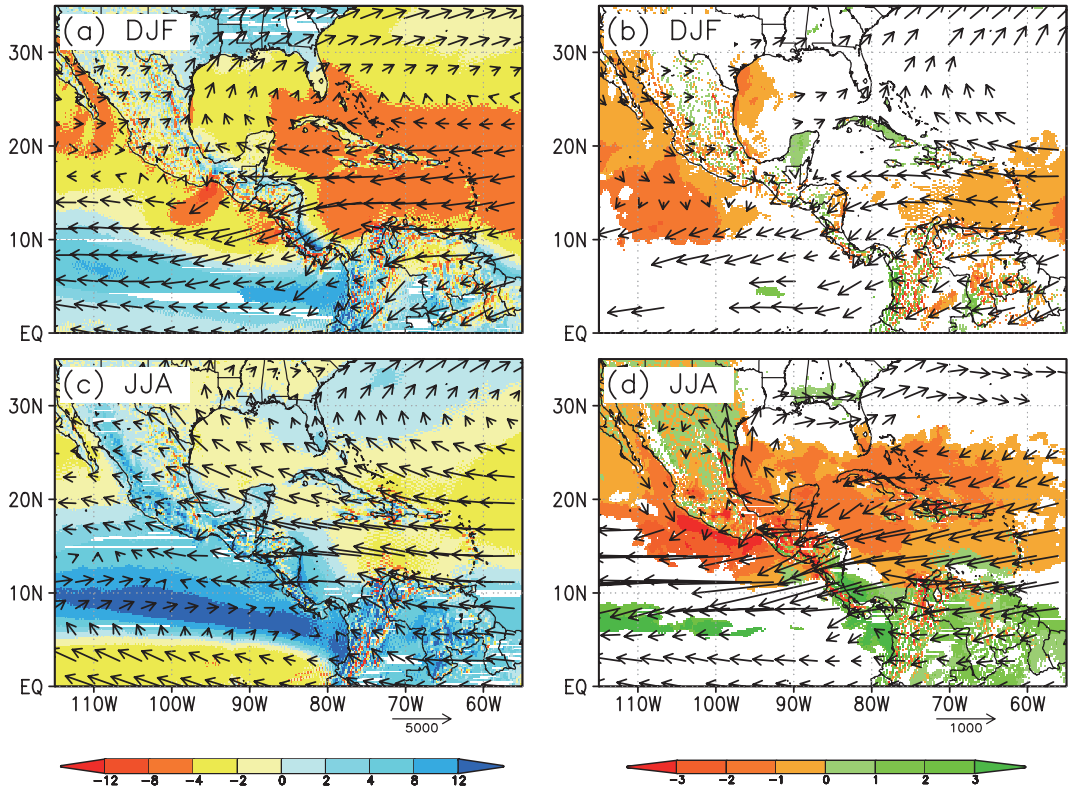

Figure 10. Present-day climatological mean vertically integrated moisture flux vectors (arrows, $\mathrm{kg\,m^{-1}\,s^{-1}}$) and their convergences (colours, $\mathrm{kg\,m^{-2}\,s^{-1}}$) in the 20-km mesh model for (a) DJF and (c) JJA, and climatological mean differences between the future and the present for (b) DJF and (d) JJA that are statistically significant at the 95% level.

CMIP3 models and is considered to be highly uncertain (IPCC, 2007). These currently unavoidable uncertainties must be taken into account in interpreting the results of our study.

6. Concluding summary

By employing the CMIP3 MME, we projected changes in the CLLJ in the future climate. The CLLJ is central to uncertainties in projections of future climate. We found that the easterly moisture flux accompanying the CLLJ would be significantly intensified in the future climate. Changes in sign were inconsistent among the CMIP3 MME, and the weighted MME mean changes were slight. The MME approach is widely regarded to be essential for general climate projections and particularly for projection of the CLLJ because the single model approach may project a biased realization of the CLLJ in the future climate among the general population.

We also performed global-scale dynamical downscaling with three horizontal resolutions. The merits of dynamical downscaling for the CLLJ and moisture flux were restricted for future climate projections, although high-resolution models showed better reproducibility of the CLLJ and moisture flux in the present-day climate than did low-resolution models Nevertheless, the high-resolution models can provided spatially detailed projections in the future climate, which is essential for impact, adaptation, and risk assessment studies in the future climate as these depend on local conditions such as topography, population, and infrastructure.

The results of the single 60- and 180-km mesh models forced by four projected SSTs demonstrate that the spatial patterns of projected SST affect the changes in the CLLJ even in a single AGCM. This reconfirms that a dynamical downscaling approach also requires multiple boundary conditions obtained from an AOGCM MME to quantify the uncertainty and that a single model is useful for exploring the mechanisms of changes in phenomena.

Both the CMIP3 MME analysis and the 60- and 180-km mesh AGCM ensembles showed that large-scale SST patterns from the eastern tropical Pacific to the Caribbean Sea to the western tropical Atlantic influence changes in the CLLJ in the future climate as similarly seen in the interannual variability of the CLLJ in the present-day climate (Wang *et al.*, 2007), demonstrating an existing underlying physical mechanism for the relationship.

An ensemble approach combining multiple GCMs and multiple RCMs has been used for future climate projections in specific regions (e.g. Giorgi *et al.*, 2009; Kendon *et al.*, 2010), and has an advantage in quantifying the uncertainty stemming from the choice of models. However, this quantification is not feasible when using a high-resolution AGCM. To overcome this drawback, we plan to perform a multi-physics ensemble experiment from different models with the same 60-km mesh model. The atmosphere–ocean interaction is a key process to

CLLJ. We also plan to perform the experiment with the atmosphere–ocean coupled version of the 60-km mesh model. These approaches should enhance our understanding of changes in phenomena and facilitate identification of the underlying physical mechanisms.

Acknowledgements

This work was funded by the Ministry of Education, Culture, Sports, Science, and Technology of Japan for the SOUSEI Program 'Projection of the change in future weather extremes using super-high-resolution AGCMs'. The Earth Simulator of the Japan Agency for Marine-Earth Science and Technology (JAMSTEC) facilitated the demanding calculations. We acknowledge the Program for Climate Model Diagnosis and Intercomparison and the World Climate Research Program's Working Group on Coupled Modeling for providing the CMIP3 multi-model dataset.

References

Angeles ME, Gonzalez JE, Erickson DJ III, Herńandez JL. 2007. Predictions of future climate change in the Caribbean region using global general circulation models. *International Journal of Climatology* **27**: 555–569. DOI: 10.1002/joc.1416

Bengtsson L, Botzet M, Esch M. 1996. Will greenhouse gas induced warming over the next 50 years lead to higher frequency and greater intensity of hurricanes? *Tellus* **48A**: 57–73.

Blázquez J, Nuñez MN. 2013. Performance of a high resolution global model over southern South America. *International Journal of Climatology* **33**: 904–919. DOI: 10.1002/joc.3478

Campbell JD, Taylor MA, Stephenson TS, Watson RA, Whyte FS. 2011. Future climate of the Caribbean from a regional climate model. *International Journal of Climatology* **31**: 1866–1878. DOI: 10.1002/joc.2200

Christensen JH, Hewitson B, Busuioc A, Chen A, Gao X, Held I, Jones R, Kolli RK, Kwon W-T, Laprise R, Magaña Rueda V, Mearns L, Menéndez CZ, Räisänen J, Rinke A, Sarr A, Whetton P. 2007. Regional climate projections. In *Climate Change 2007: The Physical Science Basis. Contribution of Working Group I to the Fourth Assessment Report of the Intergovernmental Panel on Climate Change*, Solomon S, Qin D, Manning M, Chen Z, Marquis M, Averyt KB, Tignor M, Miller HL. (eds). Cambridge University Press: Cambridge; New York; 847–940.

Clement A, Baker C, Leloup J. 2010. Climate change: patterns of tropical warming. *Nature Geoscience* **3**: 8–9. DOI: 10.1038/ngeo728

Collins M, An S-I, Cai W, Ganachaud A, Guilyardi E, Jin F-F, Jochum M, Lengaigne M, Power S, Timmermann A, Vecchi G, Wittenberg A. 2010. The impact of global warming on the tropical Pacific Ocean and El Niño. *Nature Geoscience* **3**: 391–397.

Cook KH, Vizy EK. 2010. Hydrodynamics of the Caribbean low-level jet and its relationship to precipitation. *Journal of Climate* **23**: 1477–1494. DOI: 10.1175/2009JCLI3210.1

Dee DP, Uppala SM, Simmons AJ, Berrisford P, Poli P, Kobayashi S, Andrae U, Balmaseda MA, Balsamo G, Bauer P, Bechtold P, Beljaars ACM, van de Berg L, Bidlot J, Bormann N, Delsol C, Dragani R, Fuentes M, Geer AJ, Haimberger L, Healy SB, Hersbach H, Hólm EV, Isaksen L, Kållberg P, Kähler M, Matricardi M, McNally AP, Monge-Sanz BM, Morcrette J-J, Park B-K, Peubey C, de Rosnay P, Tavolato C, Thépaut J-N, Vitart F. 2011. The ERA-Interim reanalysis: configuration and performance of the data assimilation system. *Quarterly Journal of the Royal Meteorological Society* **137**: 553–597 DOI: 10.1002/qj.828.

Enfield DB. 1996. Relationships of Inter-American rainfall to tropical Atlantic and Pacific SST variability. *Geophysical Research Letters* **23**: 3305–3308. DOI: 10.1029/96GL03231

Giannini A, Cane MA, Kushnir Y. 2000. Interdecadal changes in the ENSO teleconnection to the Caribbean region and the North Atlantic Oscillation. *Journal of Climate* **14**: 2867–2879. DOI: 10.1175/1520-0442(2001)014<2867:ICITET>2.0.CO;2

Gill AE. 1980. Some simple solutions for heat-induced tropical circulation. *Quarterly Journal of the Royal Meteorological Society* **106**: 447–462. DOI: 10.1002/qj.49710644905

Giorgi F, Jones C, Asrar GR. 2009. Addressing climate information needs at the regional level: the CORDEX framework. *WMO Bulletin* **58**: 175–183.

Gray WM. 1968. Global view of the origin of tropical disturbances and storms. *Monthly Weather Review* **96**: 669–700. DOI: 10.1175/1520-0493 (1968)096<0669:GVOTOO>2.0.CO;2

Hastenrath S. 1978. On modes of tropical circulation and climate anomalies. *Journal of Atmospheric Science* **35**: 2222–2231. DOI: 10.1175/1520-0469(1978)035<2222:OMOTCA>2.0.CO;2

Hirai M, Sakashita T, Kitagawa H, Tsuyuki T, Hosaka M, Oh'izumi M. 2007. Development and validation of a new land surface model for JMA's operational global model using the CEOP observation dataset. *Journal of the Meteorological Society of Japan* **85**: 1–24.

IPCC (Intergovernmental Panel on Climate Change). 2000. *Special Report on Emissions Scenarios: A Special Report of Working Group III of the Intergovernmental Panel on Climate Change*, Nakićenović N, Swart R (eds). Cambridge University Press: Cambridge; New York; 570.

IPCC (Intergovernmental Panel on Climate Change). 2007. Climate change 2007: the physical science basis. In Contribution of Working Group I to the Fourth Assessment Report of the Intergovernmental Panel on Climate Change, Solomon S, Qin D, Manning M, Chen Z, Marquis M, Tignor KBM, Miller HL et al. (eds). Cambridge University Press: New York.

Ishizaki Y, Nakaegawa T, Takayabu I. 2010. Comparison of three Bayesian approaches to project surface air temperature changes over Japan due to global warming. *SOLA* **6**: 21–24.

Ishizaki Y, Nakaegawa T, Takayabu I. 2012. Validation of the precipitation simulated by three regional climate models and two multi-model ensemble means over Japan for the period 1985-2004 simulated by three regional climate models and two multi-model ensemble means. *Climate Dynamics* **39**: 185–206. DOI: 10.1007/s00382-012-1304-5

Kanamaru H, Kanamitsu M. 2007. Scale-selective bias correction in a downscaling of global analysis using a regional model. *Monthly Weather Review* **135**: 334–350. DOI: 10.1175/MWR3294.1

Karmalkar AV, Bradley RS, Diaz HF. 2011. Climate change in Central America and Mexico: regional climate model validation and climate change projections. *Climate Dynamics* **37**: 605–629. DOI: 10.1007/s00382-011-1099-9

Kass RE, Raftery AE. 1995. Bayes factors. *Journal of the American Statistical Association* **90**: 773–795.

Kendon EJ, Jones RG, Kjellström EK, Murphy JM. 2010. Using and designing GCM–RCM ensemble regional climate projections. *Journal of Climate* **23**: 6485–6503. DOI: 10.1175/2010JCLI3502.1

Kitoh A, Kusunoki S. 2008. East Asian summer monsoon simulation by a 20-km mesh AGCM. *Climate Dynamics* **31**: 389–401. DOI: 10.1007/s00382-007-0285-2

Kitoh A, Ose T, Kurihara K, Kusunoki S, Sugi M, KAKUSHIN Team-3 Modeling Group. 2009. Projection of changes in future weather extremes using super-high-resolution global and regional atmospheric models in the KAKUSHIN Program: results of preliminary experiments. *Hydrological Research Letters* **3**: 49–53. DOI: 10.3178/hrl.3.49

Kitoh A, Kusunoki S, Nakaegawa T. 2011. Climate change projections over South America in the late twenty-first century with the 20-km and 60-km mesh MRI-AGCM. *Journal of Geophysical Research* **116**: D06105. DOI: 10.1029/2010JD014920

Kjellstorm EK, Giorgi F. 2010. Introduction. *Climate Research* **44**: 117–119. DOI: 10.3354/cr00976

van der Linden P, Mitchell JFB. 2009. *ENSEMBLES: Climate Change and its Impacts: Summary of Research and Results from the ENSEMBLES Project*. Met Office Hadley Centre 160pp: Exeter.

Lu J, Deser C, Reichler T. 2007. Expansion of the Hadley Cell under global warming. *Geophys. Res. Lett*. **34**: 443. DOI:10.1029/2006GL028443.

Matsuno T. 1966. Quasi-geostrophic motions in the equatorial area. *Journal of the Meteorological Society of Japan* **44**: 25–42.

Meehl GA, Covey C, Delworth T, Latif M, McAvaney B, Mitchell JFB, Stouffer RJ, Taylor KE. 2007. The WCRP CMIP3 multi-model dataset: a new era in climate change research. *Bulletin of the American Meteorological Society* **88**: 1383–1394. DOI: 10.1175/BAMS-88-9-1383

Méndez M, Magaña V. 2010. Regional aspects of prolonged meteorological droughts over Mexico and Central America. *Journal of Climate* **23**: 1175–1188. DOI: 10.1175/2009JCLI3080.1

Min S-K, Hense A. 2006. A Bayesian approach to climate model evaluation and multi-model averaging with an application to global mean surface temperatures from IPCCAR4 coupled climate models. *Geophysical Research Letters* **33**: L08708. DOI: 10.1029/2006GL025779

Mizuta R, Oouchi K, Yoshimura H, Noda A, Katayama K, Yukimoto S, Hosaka M, Kusunoki S, Kawai H, Nakagawa M. 2006. 20-km-mesh global climate simulations using JMA-GSM model –Mean climate states–. *Journal of the Meteorological Society of Japan* **84**: 165–185.

Mizuta R, Adachi Y, Yukimoto S, Kusunoki S. 2008. Estimation of the future distribution of sea surface temperature and sea ice using the CMIP3 multi-model ensemble mean. Technical Report of the Meteorological Research Institute **56**: 28pp.

Mo KC, Higgins WR. 1996. Large scale atmospheric moisture transport as evaluated in the NMC/NCAR and the NASA/DAO reanalyses. *Journal of Climate* **9**: 1531–1545. DOI: 10.1175/1520-0442(1996)009<1531:LSAMTA> 2.0.CO;2

Munoz E, Busalacchi AJ, Nigam S, Ruiz-Barradas A. 2008. Winter and summer structure of the Caribbean low-level jet. *Journal of Climate* **21**: 1260–1276.

Murakami H, Wang B. 2010. Future change of North Atlantic tropical cyclone tracks: projection by a 20-km-mesh global atmospheric model. *Journal of Climate* **23**: 2699–2721. DOI: 10.1175/2010JCLI3338.1

Murakami H, Mizuta R, Shindo E. 2012. Future changes in tropical cyclone activity projected by multi-physics and multi-SST ensemble experiments using the 60-km-mesh MRI-AGCM. *Climate Dynamics* **39**: 9–10, 2569–2584. DOI: 10.1007/s00382-011-1223-x

Nakaegawa T, Vergara W. 2010. First projection of climatological mean river discharges in the Magdalena River Basin, Colombia, in a changing climate during the 21st century. *Hydrological Research Letters* **4**: 50–54. DOI: 10.3178/hrl.4.50

Nakaegawa T, Kitoh A, Murakami H, Kusunoki S. 2013a. Annual maximum 5-day rainfall total and maximum number of consecutive dry days over Central America and the Caribbean in the late 21st century projected by an atmospheric general circulation model with three different horizontal resolutions. *Theoretical and Applied Climatology*. DOI: 10.1007/s00704-013-0934-9

Nakaegawa T, Kitoh A, Hosaka M. 2013b. Discharge of major global rivers in the late 21st century climate projected with the high horizontal resolution MRI-AGCMs -overview-. *Hydrological Processes* **27**. DOI: 10.1002/hyp.9831

Neelin JD, Münnich M, Su H, Meyerson JE, Holloway CE. 2006. Tropical drying trends in global warming models and observations. *Proceedings of the National Academy of Sciences of the United States of America* **103**: 6110–6115. DOI: 10.1073/pnas.0601798103

Onogi K, Tsutsui J, Koide H, Sakamoto M, Kobayashi S, Hatsushika H, Matsumoto T, Yamazaki N, Kamahori H, Takahashi K, Kadokura S, Wada K, Kato K, Oyama R, Ose T, Mannoji N, Taira R. 2007. The JRA-25 reanalysis. *Journal of the Meteorological Society of Japan* **85**: 369–432.

Randall D, Pan D-M. 1993. Implementation of the Arakawa-Schubert cumulus parameterization with a prognostic closure. Meteorological monograph/the representation of cumulus convection in numerical models. *Journal of Atmospheric Science* **46**: 137–144.

Rauscher SA, Giorgi F, Diffenbaugh NS, Seth A. 2008. Extension and intensification of the Meso-American mid-summer drought in the twenty-first century. *Climate Dynamics* **31**: 551–571. DOI: 10.1007/s00382-007-0359-1

Rauscher SA, Kucharski F, Enfield DB. 2011. The role of regional SST warming variations in the drying of Meso-America in future climate projections. *Journal of Climate* **24**: 2003–2016. DOI: 10.1175/2010JCLI3536.1

Rayner NA, Parker DE, Horton EB, Folland CK, Alexander LV, Rowell DP, Kent EC, Kaplan A. 2003. Global analyses of sea surface temperature, sea ice, and night marine air temperature since the late nineteenth century. *Journal of Geophysical Research* **108**: 4407. DOI: 10.1029/2002JD002670

Ropelewski CF, Halpert MS. 1987. Global and regional scale precipitation patterns associated with the El Niño/Southern Oscillation. *Monthly Weather Review* **115**: 1606–1626.

Salazar LF, Nobre CA, Oyama MD. 2007. Climate change consequences on the biome distribution in tropical South America. *Geophysical Research Letters* **34**: L09708. DOI: 10.1029/2007GL029695

Sellers PJ, Mints Y, Sud YC, Dalcher A. 1986. A simple biosphere model (SiB) for use within general circulation models. *Journal of the Atmospheric Sciences* **43**: 505–531.

Serra YL, Kiladis GN, Hodges KI. 2010. Tracking and mean structure of easterly waves over the Intra-Americas sea. *Journal of Climate* **23**: 4823–4840. DOI: 10.1175/2010JCLI3223.1

Singh B. 1997. Climate changes in the Greater and southern Caribbean. *International Journal of Climatology* **17**: 1093–1114.

Taylor MA, Whyte FS, Stephenson TS, Campbell JD. 2012. Why dry? Investigating the future evolution of the Caribbean low level jet to explain projected Caribbean drying. *International Journal of Climatology* **32**: 119–128. DOI: 10.1002/joc.3461

Tebaldi C, Smith RL, Nychka D, Mearns LO. 2005. Quantifying uncertainty in projection of regional climate change: a Bayesian approach to the analysis of multimodel ensembles. *Journal of Climate* **18**: 1524–1540.

Wang C, Lee S-K, Enfield DB. 2007. Impact of the Atlantic warm pool on the summer climate of the western hemisphere. *Journal of Climate* **20**: 5021–5040. DOI: 10.1175/JCLI4304.1

Wang C, Lee S, Enfield D. 2008. Climate response to anomalously large and small Atlantic warm pools during the summer. *Journal of Climate* **21**: 2437–2450.

Whyte FS, Taylor MA, Stephenson TS, Campbell JD. 2008. Features of the Caribbean low level jet. *International Journal of Climatology* **28**: 119–128. DOI: 10.1002/joc.1510

Xie S-P, Deser C, Vecchi GA, Ma J, Teng H, Wittenberg AT. 2010. Global warming pattern formation: sea surface temperature and rainfall. *Journal of Climate* **23**: 966–986. DOI: 10.1175/2009JCLI3329.1

